The SVD Beamformer: Physical Principles and Application to Ultrafast Adaptive Ultrasound

Hanna Bendjador, Thomas Deffieux, and Mickaël Tanter

Abstract—A shift of paradigm is currently underway in biomedical ultrasound thanks to plane or diverging waves coherent compounding for faster imaging. One remaining challenge consists in handling phase and amplitude aberrations induced during the ultrasonic propagation through complex layers. Unlike conventional line-per-line imaging, ultrafast ultrasound provides backscattering information from the whole imaged area for each transmission. Here, we take benefit from this feature and propose an efficient approach to perform fast aberration correction. Our method is based on the Singular Value Decomposition (SVD) of an ultrafast compound matrix containing backscattered data for several plane wave transmissions. First, we explain the physical signification of SVD and associated singular vectors within the ultrafast matrix formalism. We theoretically demonstrate that the separation of spatial and angular variables, rendered by SVD on ultrafast data, provides an elegant and straightforward way to optimize the angular coherence of backscattered data. In heterogeneous media, we demonstrate that the first spatial and angular singular vectors retrieve respectively the non-aberrated image of a region of interest, and the phase and amplitude of its aberration law. Numerical, *in vitro* and *in vivo* results prove the efficiency of the image correction, but also the accuracy of the aberrator determination. Based on spatial and angular coherence, we introduce a complete methodology for adaptive beamforming of ultrafast data, performed on successive isoplanatism patches undergoing SVD beamforming. The simplicity of this method paves the way to real-time adaptive ultrafast ultrasound imaging and provides a theoretical framework for future quantitative ultrasound applications.

Index Terms— Adaptive Beamforming, Ultrafast Imaging, Singular Value Decomposition, Aberration Correction.

I. INTRODUCTION

ALTHOUGH ultrasound imaging is a mature medical imaging tool, new techniques are constantly explored to further improve image quality and extend its clinical

usefulness to new applications. The first objective of Ultrasound imaging is to build an accurate image of the medium from ultrasonic backscattered signals through a process called beamforming.

It can be expressed as an inverse problem between the received ultrasonic echoes and the acoustic impedance distribution in the medium. This inverse problem is easily solved when assuming the local speed of sound and density to be constant in the medium.

This hypothesis is accepted in all conventional clinical devices and led to the standard Delay-And-Sum beamforming process. In practice, it consists in computing and correcting the time-of-flight for different travel paths between each pixel and each transducer array element. In order to form high quality images at higher frame rates, ultrafast plane wave compound imaging [1]–[7] was introduced. It gave rise to a wide range of applications such as Shear Wave Elastography, Ultrafast Doppler, Functional Neuroimaging or Quantitative Ultrasound imaging [8]. However, similarly to conventional imaging, image quality can still suffer from sound speed heterogeneities in the medium; leading sometimes to non-negligible phase aberrations on propagating wavefronts [9]. Such aberrations affect the image itself but also the ensuing quantitative estimations in post-processing steps.

In the last thirty years, many different approaches have been developed to address this issue but this topic remains highly relevant today despite longstanding research efforts. Measurement of the transmit echo phase [10] in Computed Ultrasound Tomography [11] informs on the arrival time of the transmitted wave front and allows correction of small aberrations compared to the PSF width. In conventional ultrasound, we are limited to the use of backscattered signals and the ultimate goal of aberration correction is actually to recreate an equivalent point-like scatterer for each pixel of the image. Then, the phase and amplitude distortion of its spherical backscattered echo retrieve the so called Green's function [12]. When no bright reflector is available but rather a random distribution of Rayleigh scatterers, time-reversal of this speckle noise [13], [14] can be used to virtually recreate an artificial ultrasonic star, whose echo retrieves the aberration laws. Though, it remains an iterative and quite complex non real-time process. Other approaches studying the spatial coherence of backscattered signals can be exploited to optimize the summation of the different plane waves in

beamforming [15]. In speckle noise environment which is the vast majority of configurations assessed in Biomedical Ultrasound, Van Cittert Zernike theorem states indeed that this spatial coherence measures the focusing quality [16], which is essential for an accurate ultrasound image. Founded on the use of this theorem, coherence-based imaging methods [17] were developed to improve image quality, especially Contrast-to-Noise and Signal-to-Noise ratio, due to speckle reduction techniques. All these methods improving spatial coherence were shown to decrease aberration across an aperture. In particular, Dahl and Trahey [18] proposed an imaging technique based on the pixel mapping of this spatial coherence of ultrasound signals. This short-lag spatial coherence method (SLSC) consists in estimating the spatial coherence between closely-spaced elements to create images demonstrating superior SNR and CNR compared to conventional ultrasound images. SLSC permits to improve the spatial coherence of backscattered signals by using only data demonstrating a strong angular coherence for different compounded transmissions without trying to estimate the aberration law [19]. This efficient approach requires the estimation of spatial coherence functions on a pixel per pixel basis whose computational cost currently hampers a real-time implementation [20]–[22]. It was also recently expanded to angular coherence in the context of compounded plane waves [23].

Here, we propose a different approach to improve the ultrasonic image quality. Our method shares the common aim to increase the angular coherence of signals coming from each pixel for different transmits during plane wave compound imaging. This new approach offers a fast and efficient correction process, both retrieving an optimized ultrasonic image and the local estimation of the amplitude and phase of the aberrations. Additionally, it also filters out low coherence signals from the data.

Moreover, the technique keeps the data in the conventional beamformed data space allowing to subsequently perform any conventional ultrasound estimation such as phase estimation, power Doppler, or pulsed Doppler.

Importantly, we introduce the Ultrafast Compound Matrix containing images, both beamformed in the receive mode and phase delayed for transmit travel path compensation. We explain theoretically the physical meaning of its Singular Value Decomposition. In complement to former works applying SVD to subaperture or synthetic transmit data [15], [24], [25], we hereby demonstrate a theoretical link between the SVD of beamformed data from different transmissions and the local ultrasonic aberrations. Finally, we propose a complete real-time adaptive beamforming technique for ultrafast imaging based on the application of SVD beamforming on subsets of the Ultrafast Compound Matrix corresponding to isoplanatic patches. This SVD beamformer merges Phase Aberration Correction (PAC) techniques and coherence-based imaging approaches in a unique matrix formalism implementation. Results of this novel and fast method in simulations, *in vitro* phantoms and *in vivo* liver experiments are presented.

II. THEORY AND PHYSICAL INTERPRETATION OF ULTRAFAST ULTRASOUND BEAMFORMING

A. Basic Principles of Ultrasound Imaging Inverse Problem

Considering a transducer array made of N_e elements, and a medium containing a random distribution of K scatterers (Rayleigh diffusion with $K \gg N_e$), we define a dimensionless scattering amplitude β_{ik} characterizing the kth scatterer illuminated by the ith transducer. Let $h_{k,i}$ be the temporal impulse response defining the propagation between a transducer element i and a scatterer k. Thanks to spatial reciprocity, the temporal impulse response $h_{j,k}$ defining the propagation between the scatterer k and the transducer element j is equal to $h_{k,j}$. Let $e_i(t)$ be the emitted signal on the ith transducer, the received signal on an element j can be expressed as:

$$s_j(t) = \sum_{i=1}^{N_e} \sum_{k=1}^{K} \beta_{ik} * h_{j,k}(t) * h_{k,i}(t) * e_i(t) \quad (1)$$

where $*$ stands for the convolution operation [26]. As the spatial resolution of the ultrasound image is limited by the ultrasonic wavelength, it is convenient to introduce a discrete representation of the ultrasound-formed image, with a spatial pitch of the order of the ultrasonic wavelength. Each pixel $p = (p_x, p_z)$ contains a subset of $\{K_p\}$ scatterers. For each subset, we notice that the travel time, for a given scatterer k, can be written as: $\tau_{p,k} = \tau_p + \Delta\tau_k$, with $\Delta\tau_k \ll \tau_p$. Equation (1) becomes:

$$s_j(t) = \sum_{i=1}^{N_e} \sum_{p=1}^{N_x N_z} \sum_{k \in \{K_p\}} \beta_{ik} * h_{j,p}(t - \tau_p) * \delta(t - \Delta\tau_k)$$
$$* h_{p,i}(t - \tau_p) * \delta(t - \Delta\tau_k) * e_i(t)$$
$$= \sum_{i=1}^{N_e} \sum_{p=1}^{N_x N_z} h_{j,p}(t) * h_{p,i}(t) \underbrace{\sum_{k \in \{K_p\}} \beta_{ik} \delta(t - 2\Delta\tau_k)}_{\gamma_{ip}(t)} \quad (2)$$

where $\gamma_{ip}(t)$ is a backscattering function describing the reflection induced by the scatterers distribution in pixel p when insonified by the transmit element i. Thus, the received signal becomes:

$$s_j(t) = \sum_{i=1}^{N_e} \sum_{p=1}^{N_x N_z} \gamma_{ip}(t) * h_{j,p}(t) * h_{p,i}(t) * e_i(t) \quad (3)$$

The difference between the equation (3) and the equation (1) lies in the introduction of a backscattering function $\gamma_{ip}(t)$ for each pixel, instead of a simple scalar value β_{ik} for each scatterer. This function characterizes the spatial dependence of the scattering coming from a given pixel of the image. This formalism no longer requires a Green's function per scatterer, but only one for each pixel. Since the number of pixels ($N = N_x N_z$) is far below the number of scatterers in the medium (K), this strongly simplifies the calculations.

Depending on the strength and distribution of scatterers in each pixel of the ultrasonic image, the scattering functions

$\gamma_{ip}(t)$ can be very different. If pixel p contains only a strong point-like reflector, the scattering function $\gamma_{ip}(t)$ is independent of the transmit element i. In that case, $\gamma_{ip}(t) = \gamma_p(t)$ and all backscattered signals coming from pixel p are coherent. Their spatial coherence function is thus a square function. If the pixel p contains a random distribution of Rayleigh scatterers, the function $\gamma_{ip}(t)$ is different for each transmission coming from different transmit elements. The spatial coherence function of backscattered signals coming from pixel p is then a triangle function according to the Van Cittert Zernike theorem [16].

The ultimate objective of ultrasound imaging is to solve the inverse problem of ultrasound propagation, in order to retrieve all $\gamma_{ip}(t)$ functions for each pixel p. Solving this problem requires to retrieve all Green's functions $h_{pi}(t)$ relating each pixel p to each element i of the ultrasonic array. When pixel p contains a point-like reflector, the Green's function $h_{pi}(t)$ can be retrieved by applying the concept of iterative time reversal focusing [27] or using the decomposition of the time reversal operator [26]. When pixel p contains a random distribution of Rayleigh scatterers, it becomes much more complex to estimate $h_{pi}(t)$. Indeed, due to the inherent speckle noise nature of backscattered signals, the scattering function $\gamma_{ip}(t)$ is dependent on the transmit element i. This fundamental limit makes the inverse problem of ultrasound imaging difficult to solve in speckle noise environment. Unfortunately, speckle noise configuration corresponds to the vast majority of bio-medical ultrasound imaging.

Indeed, in speckle noise, retrieving $h_{pi}(t)$ requires to recreate a single virtual point-like reflector in each pixel p of the image, and to separate the contribution of each pixel in the backscattered signals. Recreating such a virtual point-like reflector from speckle noise consists in increasing the spatial coherence of its backscattered signals from a triangle function to a square function. Thus, the problem of creating virtual point-like scatterers can be seen as maximizing the spatial coherence of backscattered signals coming from each focal spot. For this reason, the ultimate goal of ultrasound imaging can be seen as maximizing the spatial coherence function of backscattered signals, coming from all pixels or focal spots. Thus, this enables to retrieve each Green's function associated to each pixel (Fig.1).

B. Fourier Domain: Beamforming and Adjoint Operator

In the Fourier domain, convolution turns out to be a matrix product and equation (3) can be rewritten as:

$$S(\omega) = H(\omega)\Gamma(\omega)\,{}^tH(\omega)E(\omega) \qquad (4)$$

For a sake of clarity, we will consider in the following demonstration that $S = S(\omega_0)$, where ω_0 is the central frequency of the transmitted pulse. We introduce the same notation simplification for all vectors and matrices in the following sections of the paper. Let us introduce a model of the propagation between each element of the ultrasonic array and each pixel of the image. This propagation model can be defined as a propagation operator H_0 as similar as possible to the true propagation operator H. The beamforming operation
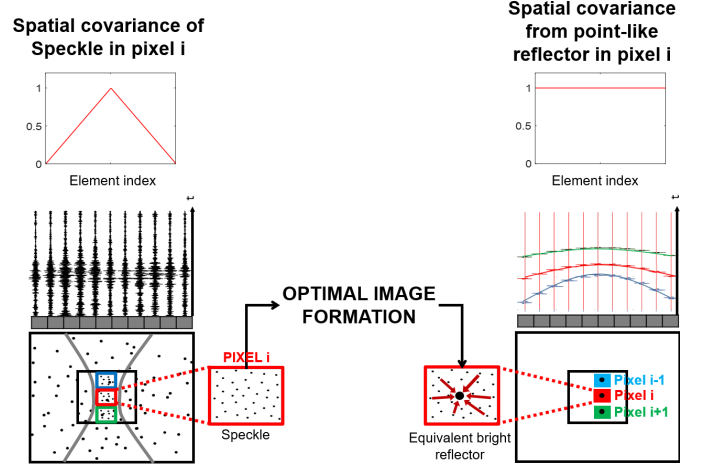

Fig. 1. Schematic description of the general aim of ultrasound imaging: Most scattering in biomedical ultrasound comes from random distribution of Rayleigh scatterers. i.e. the speckle noise. For each pixel, the inverse problem, or beamforming, consists in retrieving from this speckle noise the signature of an equivalent single point-like reflector. The scattering of such point-like reflector gives access to the local Green's function of the pixel.

in the receive mode, consists in estimating

$$I = {}^tH_0^*H\Gamma\,{}^tHE \qquad (5)$$

I is a $[N_x N_z, 1]$-vector, corresponding to the image for a transmission vector E. The symbol $*$ corresponds to the phase conjugate operator.

In the case where H_0 is equal to H, ${}^tH_0^*H \approx Id$ where Id is the Identity Matrix, and $I = \Gamma\,{}^tHE$. Thus, the beamformed image I corresponds to the exact image of Γ, where each pixel has been multiplied by an amplitude and phase contained in the vector ${}^tHE$, describing the travel time path differences during forward propagation from the array to the pixels.

In experimental configurations due to diffraction limits, it is known that ${}^tH_0^*H$ is not perfectly equal to the identity matrix, but rather estimates the point spread functions. Indeed, in each ith column of ${}^tH_0^*H$, we find the point spread function of the focusing in the ith pixel [28]–[31]. So, if H_0 is almost equal to H, we can introduce the Point Spread function Matrix Ps:

$$
{}^tH_0^*H = \begin{bmatrix} & & 0 \\ & \diagdown & \\ 0 & & \end{bmatrix} = Ps \qquad (6)
$$

where all columns of Ps describe the point spread functions for each individual pixel focal spot of the experimental configuration: the ith column vector of Ps corresponds to the ith pixel's PSF.

C. Conventional vs Plane Wave Imaging

In conventional imaging, the focusing in the transmit mode is performed by successive transmissions of transmit vectors $E_i = {}^tH_{0,p}^*$, where $H_{0,p}$ is the pth column of H_0. ${}^tH_{0,p}^*$ is the phase conjugate of the Green's function ${}^tH_{0,p}$ and thus represents a transmit vector focusing on pixel p. For each
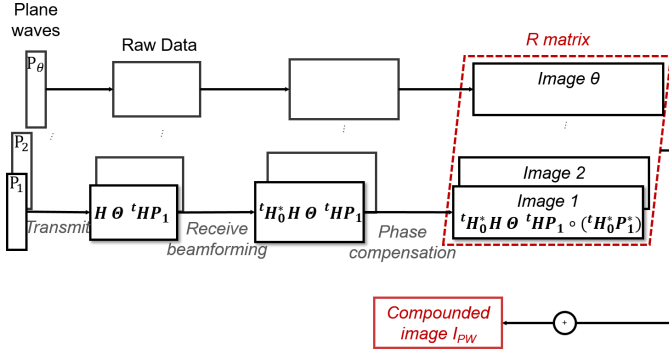
Fig. 2. Matrix description of beamforming in coherent compounding: definition of the Ultrafast Compound Matrix R and the Plane wave imaging matrix IPW. The Hadamard product describes the coherent compounding before the final summation on the transmit angles: term-to-term product with ${}^tH_0^*P^*$ compensates phases delays and amplitudes between transmitted plane waves.

transmit, the final image I_m is the diagonal of the matrix I defined in Fig. 2:

$$I_m = diag(I) = diag({}^tH_0^*H\Gamma {}^tH {}^tH_0^*) \tag{7}$$

In compounded plane wave imaging, the focusing is performed by a set of $N_\theta > 1$ plane wave transmissions. For our matrix formalism, this requires to introduce a Matrix P representing the change of referential basis between the canonical space (array elements) and the plane wave space. So P is a $[N, N_\theta]$ matrix. The final image obtained in plane wave compounding is thus quite similar to the conventional image described in equation (7) with a potential filtering described by $P {}^tP^*$ when the number of plane waves is lower than the number of elements:

$$I_m = diag(I_{PW}) = diag({}^tH_0^*H\Gamma {}^tHP {}^tP^* {}^tH_0^*) \tag{8}$$

D. The Ultrafast Compound Matrix R

We now choose to introduce an important matrix in compound plane wave imaging: the ultrafast compound data matrix R. It contains the N_θ images beamformed in the receive mode and individually time delayed pixel per pixel depending on their transmit angle. R is thus a $[N_x N_z, N_\theta]$ matrix. It corresponds to the matrix of compounded plane wave data right before the final summation on angles, which is the last operation in ultrafast data beamforming to retrieve the coherent compounded image. As done earlier, we note the number of pixels $N = N_x N_z$. R can be written as:

$$R = ({}^tH_0^*H\Gamma {}^tHP) \circ ({}^tH_0^*P^*) \tag{9}$$

where $\circ$ stands for the matrix Hadamard product (Fig. 2).

Let us define A_e, the $[N_e, N_e]$ matrix describing a physical realistic aberrator in the canonical basis (array elements space). Assuming that the aberrator does not dramatically affect transmit focusing, the ultrafast compound matrix R can be defined as follows:

$$R = ({}^tH_0^*H\Gamma {}^tHA_eP) \circ ({}^tH_0^*P^*) \tag{10}$$

We introduce A_θ as the angular aberration matrix describing these aberrations in the plane wave basis. It is related to A_e through the former matrix P of dimension (N_e, N_θ) describing the projection from canonical space to plane wave space.

As long as the number of independent angles N_θ (independent meaning $\forall i, \forall j \langle P_i \mid P_j \rangle = 0$) is sufficient to describe any kind of ultrasonic wavefield initially defined in the canonical basis, the matrix P is invertible [29]. In that case, we have $A_\theta = P^{-1}A_eP$ and the angular aberration matrix A_θ is related to A_e thanks to:

$$PA_\theta = A_eP \tag{11}$$

Combining (10) and (11), the ultrafast compound matrix R can be rewritten using the angular aberration matrix as:

$$R_\theta = ({}^tH_0^*H\Gamma {}^tH_0PA_\theta) \circ ({}^tH_0^*P^*) \tag{12}$$

However, when $N_\theta \ll N_e$, P is no longer invertible and A_θ is only an approximation of the true aberration projected on the limited number of plane waves. In that case, $R_\theta \neq R$ and R_θ is only an approximation of the true ultrafast compound matrix R.

Let us now consider a homogeneous medium with a phase aberrating screen in the canonical basis. Consequently, the aberrator A_e is a $[N_e, N_e]$ diagonal matrix. When P^{-1} is defined and the phase aberrator does not contain very high spatial frequency variations in the canonical space (which is typically the case in medical ultrasound), A_θ can also be approximated by a $[N_\theta, N_\theta]$ diagonal matrix. In the following equation and under the previous hypothesis, we will note $A = A_\theta$, whose elements are $a = diag(A_\theta) = (a_i)_{i=1..N_\theta}$.

The Hadamard product is a distributive operator, which is also commutative for diagonal matrices (commutative ring of $\mathcal{M}(\mathbb{C})$). Indeed, if A and B are $\{m*n\}$-matrices, and D and E diagonal matrices of respective size m and n, it can be demonstrated that:

$$D(A \circ B)E = (DAE) \circ B = (DA) \circ (BE) = A \circ (DBE)$$

Thanks to this property, Equation (12) becomes:

$$R = ({}^tH_0^*H\Gamma {}^tH_0PA) \circ ({}^tH_0^*P^*)$$
$$= ({}^tH_0^*H\Gamma {}^tH_0P) \circ ({}^tH_0^*P^*) A$$

This results in $R = M.A$, where we define the matrix M as:

$$M = ({}^tH_0^*H\Gamma {}^tH_0P) \circ ({}^tH_0^*P^*) \tag{13}$$

Interestingly, the columns of the matrix M correspond to the ideal image of the medium, without any aberration, for each plane wave transmit. Note that the travel path differences in the transmit phase have been compensated in M. The ability to describe the matrix R as a product between ideal images M and a diagonal Matrix A will be important in the next sections.

E. The Local Angular Coherence Matrix C_θ

In order to optimally correct ultrasound images, we intend to maximize the coherence of backscattered echoes between plane wave transmits, as in [23]. For this reason, we introduce a Local Angular Coherence Matrix C_θ. First, we choose a
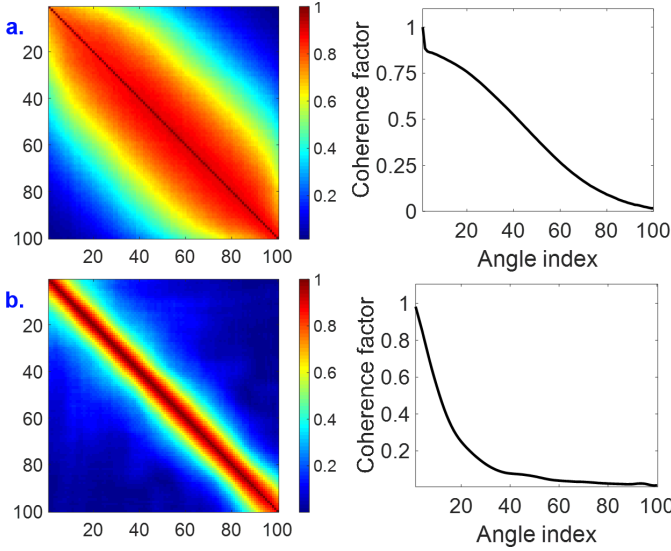
Fig. 3. Measurement of the complex magnitude of the angular coherence matrix C_θ module in a control region of interest using the Ultrafast compound Matrix $\tilde{R}$ extracted from R. $\tilde{R}$ is acquired in (a) non-aberrated and (b) aberrated speckle noise using 100 transmit compound angles. On the right side, diagonal terms are averaged and plotted, representing the angular coherence factor.

control region of interest (ROI) in the image where we would like to control the angular coherence of backscattered signals. We extract the local Ultrafast Compound matrix $\tilde{R}$ of this ROI. The angular coherence of this region of interest is retrieved by calculating the covariance matrix:

$$C_\theta = {}^t\tilde{R}^* . \tilde{R} \qquad (14)$$

Fig. 3 shows the computation of C_θ using experimental data in the case of a speckle environment in the region of interest. We will later discuss the influence of the ROI size. We notice that the anti-diagonal terms exhibit the triangle-shaped coherence expected with Van Cittert Zernike theorem. When the same medium is now imaged through an aberrating lens, the coherence vanishes. This witnesses the strength of the speckle coherence criterion in aberration correction. The complex magnitude of this correlation matrix informs on the angular coherence between ultrasonic images acquired with different plane wave transmits summed over all pixels of the region of interest. In speckle noise, as seen before, we expect it to decrease linearly as the angle difference increases.

F. The Singular Value Decomposition of the Ultrafast Compound Matrix

The estimation of the angular aberration matrix A is essential to perform proper adaptive imaging. From the definition of A, assumed to be diagonal, RA^* corresponds to the corrected image. We just demonstrated that its angular covariance has to be optimal. So, compensating for the aberrations consists in finding the correction vector X that maximizes the angular covariance of the image RX. This solution will verify $X = diag(A^*)$. We are trying therefore to maximize

the Rayleigh quotient:

$$J(X) = \frac{{}^t(RX)^* . (RX)}{X^* . X} = \frac{{}^tX^* \left({}^tR^* R\right) X}{\|X\|}$$

One notable property of the Rayleigh quotient is that it is maximized by the first eigen vector of the matrix $\left({}^tR^* R\right)$. $\left({}^tR^* R\right)$ being a Hermitian matrix, we also know that its eigen vectors are the singular vectors of the matrix R. So, this demonstrates that the first singular vector of R maximizes the angular covariance of the beamformed data, and thus corresponds to the aberration correction $diag(A^*)$. This demonstrates the striking importance of the Singular Value Decomposition of the Ultrafast Compound Matrix: $R = U S {}^tV^*$. The Rayleigh quotient optimization tells us that $diag(A^*) = V_1$, where V_1 is the first singular vector, ie the first column of V.

If we approximate ${}^tH_0{}^* H \approx Id$, we consider the PSF being limited to the focal point and not affecting neighboring pixels, the previous matrix M in equation (12) becomes:

$$M = \left(\Gamma {}^tH_0 P\right) \circ \left({}^tH_0^* P^*\right) = \Gamma . {}^tH_0 P \circ {}^tH_0^* P^*$$

$$= \Gamma . \begin{bmatrix} 1 & - & 1 \\ | & | & | \\ 1 & - & 1 \end{bmatrix} = \begin{bmatrix} \Gamma_1 & - & \Gamma_1 \\ \Gamma_2 & \vdots & \Gamma_2 \\ \vdots & \vdots & \vdots \\ \Gamma_N & - & \Gamma_N \end{bmatrix} \qquad (15)$$

All columns of M are identical, and we can write:

$$R = m \ {}^ta = \begin{bmatrix} m_1 \\ \vdots \\ m_N \end{bmatrix} . \begin{bmatrix} a_1 & \cdots & a_{N_\theta} \end{bmatrix} \qquad (16)$$

where m is the vector of the columns of M.

Such angular and spatial variables separation in equation (16) exactly corresponds to the definition of the SVD. Indeed, let's write the SVD of our ultrafast compound matrix R: $R = U S {}^tV^* = \sum_{i=1}^{N} s_{ii} u_i {}^tv_i^*$ where S is a diagonal matrix.

As $R = m \ {}^ta$, we have here:

$$s_{11} = |\bar{m}| . |a| , \quad s_{ii} = 0 \quad \forall i > 1$$
$$v_1 = \frac{a^*}{|a|}; \quad u_1 = \frac{\bar{m}}{|\bar{m}|} \qquad (17)$$

v_1 is the phase conjugate of the aberration vector a. u_1 is the normalized image in a non-aberrated medium: all pixels are seen the same way for each plane wave transmission. In this case, it is trivial that the decomposition of R is the SVD since all further singular vectors are zero, and thus orthogonal to the first one.

If we no longer consider the PSF being a spatial Dirac, and add speckle noise in the media, ${}^tH_0{}^* H \neq Id$ and the columns of M are no longer identical. There is thus an angular dependence of the imaged medium with respect to the insonification angle. We can introduce the averaged PSF: $\overline{m_i} = \frac{1}{N_\theta} \sum_{j=1}^{N_\theta} m_{ij}$. The elements of M can be written: $m_{ij} = \overline{m}(i) + \Delta m_i(\theta_j), \forall i = 1..N, \forall j = 1..N_\theta$.

If we consider the angular dependence of the point spread function to be reasonable, by assuming $\frac{|\Delta m_i|}{|\overline{m}|} \ll 1$, we can
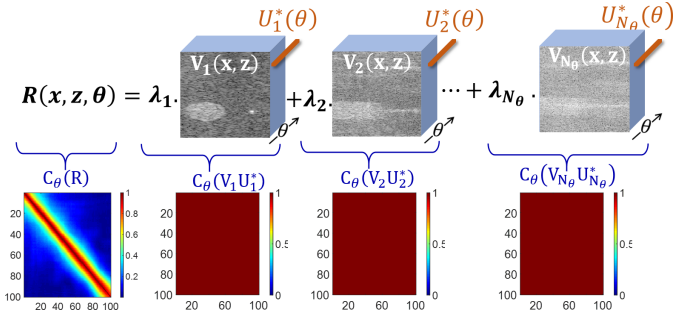
Fig. 4. Singular Value Decomposition of the Ultrafast Compound Matrix. Absolute value of angular Coherence matrix of R shows speckle decorrelation, whereas singular vectors exhibit individually an optimized angular coherence.

write:

$$R = M.A = \left[\overline{m}\,(i) + \Delta m_i\,(\theta_j)\right]_{ij} .A$$
$$= \left[a_j \overline{m}\,(i) + a_j \Delta m_i\,(\theta_j)\right]_{ij}$$
$$= \overline{m}.^t a + \Delta M.A \qquad (18)$$

And we finally get:

$$R = |\overline{m}| . |a| . \left[\frac{\overline{m}}{|\overline{m}|} . \frac{a}{|a|} + \frac{\Delta M.A}{|\overline{m}| . |a|} \right] \qquad (19)$$

with $\left| \frac{\overline{m}}{|\overline{m}|} . \frac{a}{|a|} \right| = 1$ and $\left| \frac{\Delta M.A}{|\overline{m}|.|a|} \right| \ll 1$.

Again, we know that the first singular vector of this SVD, with the highest singular value, represents the best linear fit for the rows of R. Each row of R contains the N_θ scattering complex amplitudes of one pixel seen by each individual transmit. This first singular vector maximizes the resemblance between the rows of R and the fit. In other words, the coherence between the images seen from different angles is maximized. Physically, this is equivalent to a maximization of the energy of R rows which corresponds to the highest energy of all singular vectors. As we know, due to the speckle noise features that the term $\Delta M.A$ is negligible compared to $\overline{m}.^t a$, we can again identify:

$$s_{11} = |\overline{m}| . |a| ; \quad u_1 = \frac{\overline{m}}{|\overline{m}|}; \quad v_1 = \frac{a^*}{|a|}.$$

The first singular vector of R is containing in v_1 the phase conjugate $diag(A*)$ of the aberrator. Additionally, u_1 contains the normalized image of the medium where the aberration has been corrected. All pixels behave as individual point-like reflectors with no angular dependence in transmission. For each singular vector i, one can compute the coherence matrices $C_\theta (V_i U_i^*)$, defined in part II-E. The mathematics of the SVD operation imply that these matrices are constant and equal to 1 as seen in Fig. 4. It means that, by definition, for each singular vector, all transmitted angles "see" the same image.

Interestingly, if we compute the Singular Value Decomposition of $\tilde{R}$, and re-calculate C_θ considering only the first singular vector V_1, it gives a uniform matrix equal to 1 (Fig. 4). This means that all pixels of the singular image V_1 are seen the same way for all plane wave illuminations angles due to the separation of variables achieved by the SVD. The vector U_1 contains the amplitude and phase delays between transmits,

that are required to achieve a constant coherence on the receive signal. In other words, it contains the aberration correction law of the medium acting the same way on each pixel of the region of interest. For this reason, an important point is to understand the optimal size of the control region for SVD as it is closely linked to the concept of isoplanatic patches [28], [32].

Strikingly, the Singular Value Decomposition of the Ultrafast Compound matrix gives access, with its first singular vector, to the knowledge of the aberrating screen. We notice that selecting the first vector out of the SVD is equivalent to filtering the images and re-phasing them with the phase conjugate of the aberrator A^*. Indeed, SVD filtering creates angular coherence for each point of an aberrated medium. This is the definition of creating a virtual reflector in each pixel location. This is actually the mathematical explanation for the bright reflector virtual creation in speckle noise described in [13]. The interesting and unique aspect of our method stands in the physical understanding of the way to re-create coherence in aberrated signal. The SVD-beamformer is a straightforward and non iterative solution for this complex problem addressed in [13].

One should note that the aberration was here assumed to have an effect only in the transmit mode, for a sake of simplicity in the former mathematical developments. The aberration in the receive mode can be taken into account by re-writing Equation (9) in:

$$R = \left(^t H_0^* P_0^* \Gamma A\,^t P_0\,^t H P A\right) \circ \left(^t H_0^* P^*\right)$$

where P_0 is the orthonormal $[N_e, N_e]$-matrix, changing from canonical to plane wave basis with $rank\,(P_0) = N_e$.

In ultrafast imaging, $rank\,(P_0)$ is often much greater than $rank\,(P)$ as $N_e \gg N_\theta$ in most cases. Then, likewise, we can write:

$R = M.A = \overline{m}.^t a + \Delta M.A$, and the SVD retrieves as well the aberration matrix.

III. METHODS

A. Acquisitions

Ultrasound acquisitions were performed using a 256-channel programmable research scanner (Verasonics Research Systems). We developed customized sequences to drive a 192-element linear probe, at a central frequency of 6.25 MHz and pitch size of 0.2 mm (SL10-2 probe, Supersonic Imagine, Aix-en-Provence, France). Plane waves steered at angles between $-18°$ and $+18°$ were transmitted to insonify the media. In order to guarantee the highest level of information, 100 angles at Pulse Repetition Frequency (PRF) = 10 kHz were acquired along with subsets of steering angles for higher frame rate images. A phantom containing reflecting pins, hyperechoic and anechoic cysts (CIRS 054GS – 1540 m/s) was used to assess our method, successively without and with a shaped-surface silicone aberrating lens.

B. Correction Method

Classical Delay-And-Sum beamforming - at $dx = \lambda$, $dz = \lambda/2$ - was performed on plane wave data for each
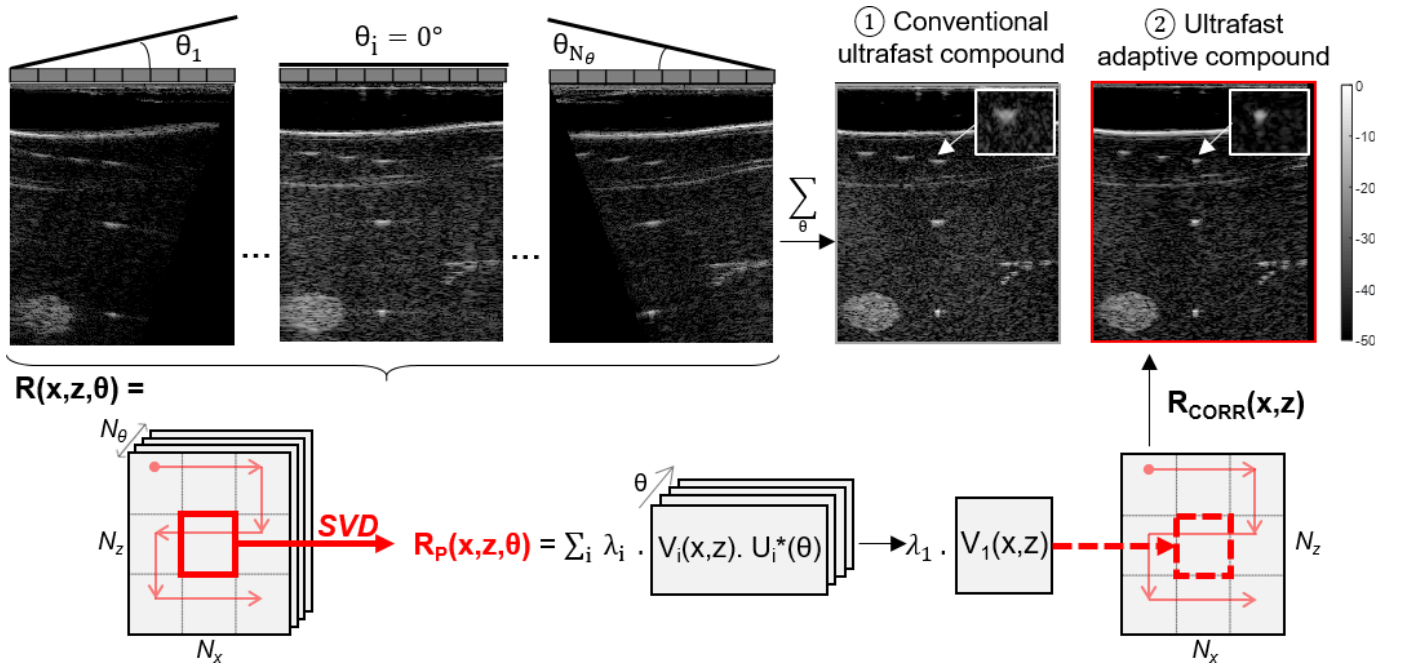
Fig. 5. Fast aberration correction and filtering with SVD. Ultrafast compound matrix R retrieves IQ data beamformed for each transmit angle. Isoplanatic patches are defined within the imaged area. SVD is performed on each patch of the image, and the first eigen vector gives directly the rephased image. Final corrected image is computed by assembling corrected patches.

steered transmit. Resulting IQ signals were stored in a 3D-matrix R: the *ultrafast compound matrix* containing (x,z)-images for each angle θ (Fig. 5①). Summation along the third dimension, gives simply the conventional plane wave compounded B-mode image.

Matrix R is reshaped into a 2D Casorati Matrix form with a $[N_x \ N_z, \ N_\theta]$ dimension. The Singular Value Decomposition is then performed on delimited spatial ROIs called "control patches", each corresponding to a smaller Ultrafast Compound matrix $\tilde{R}$. We can adapt the dimension of the control ROIs with respect to the isoplanatism limited extension induced by the aberrator. SVD of each $\tilde{R}$ matrix is performed and provides the separation of spatial and angular variables. For each singular value, the SVD consists actually in the product of images V(x,z) and angular vectors U*(θ) weighted with singular values λ. The decomposition is filtered, keeping only the image with the highest singular value. For each angle, the corrected image of each ROI is thus corresponding to $\lambda_1.V_1(x,z)$. Summing data on the different angles retrieves this corrected image (Fig. 5②). The IQ signals have been rephased with the complex $U_1(\theta)$ correction vector containing the phase and amplitude corrections. As described in part II., the first eigen vector guarantees a maximization of the angular coherence. This coherence is indeed a constant square function equal to 1, since all angles "see" the same outcome from the object.

We studied four experimental cases for comparison: the classical ultrafast compound imaging in homogeneous medium, the SVD-beamforming using experimental data incorporating a *numerical* aberration and finally *in vitro* and *in vivo* experimental data containing *physical* aberrations. The classical ultrafast compound in homogeneous medium was

considered as the goal to reach for the aberrated images correction by the SVD beamformer.

We call *numerical* aberration, the introduction at emission on acquired data, of a known angular delay law (Fig. 6) and we evaluated the consistency between the phase aberration determined with our method, and the expected one. We also introduced *physical* aberrations: between the probe and the phantom, we placed a silicone aberrating lens and applied the SVD beamformer to compensate this near-field aberrator in the corrected image (Fig. 7). Finally, *in vivo* experiments were conducted in the human liver where aberrations are more spatially distributed.

In all experiments, many patch sizes were tested and the final result was obtained with the largest patch keeping the consistency of the aberrator in both *x* and *z* dimensions.

Quantification of the image quality can be found in the angular coherence matrix, which mathematically becomes constant and maximal between all angles after correction. Though, we can also provide classical estimators such as lateral resolution – computed by the half width lateral resolution of a reflecting pin intensity, and contrast defined by: $= \frac{\mu_i}{\mu_o}$, where $\mu_i = \bar{s}_i^2$ and $\mu_o = \bar{s}_o^2$ are the mean square intensities respectively inside (*i*) and outside (*o*) an anechoic cyst.

IV. RESULTS

A. SVD Beamforming in Speckle Noise With Numerical Aberrators

If one computes the angular coherence in speckle for a casual B-mode image, limited to a control region, the obtained matrix exhibits a triangle profile: covariance is maximal along
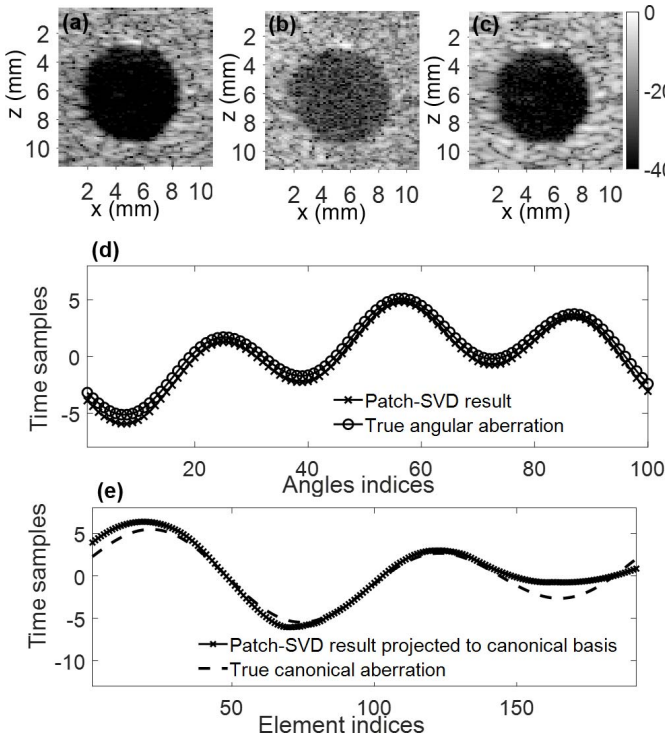
Fig. 6. (a) Bmode image of a CIRS 054-GS phantom anechoic cyst. (b) Example of image after introduction of an angular numerical aberration in transmit. (c) Same image as (b) after SVD-beamformer. (d) Example of simulated angular aberration: SVD-beamforming result is compared to the true aberration introduced. (e) Example of simulated canonical laws: SVD-beamforming result is projected in the element-space and then compared to the true canonical aberration introduced.
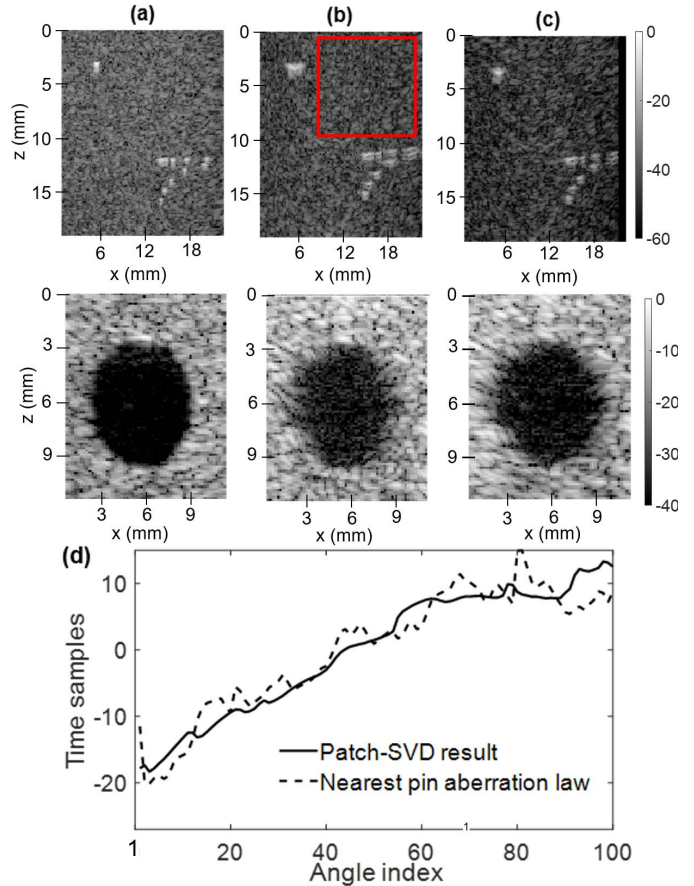

Fig. 7. (a) Bmode images of a CIRS 054-GS phantom reflecting pins and anechoic cyst. (b) Images after propagation through an aberrating lens. (c) Images after SVD-beamformer. (d) Aberrating laws: extracted from SVD-beamforming on a patch, and from the closest pin echo.

the diagonal – auto-coherence - and vanishes linearly down to zero when the angular spacing increases (Fig. 3).

Van Cittert Zernike theorem stipulates actually that the shape of the spatial coherence is driven by the inverse Fourier transform of the focal spot intensity. The focal spot intensity varies as sinc^2, which is the Fourier Transform of a triangle function. Indeed in speckle, one obtains a linear decrease in spatial coherence as much as the lag between elements increases. This theory is transposable when it comes to angular coherence and transmit angular lag, as demonstrated in reference [23]. This explains the evolution of angular coherence of backscattered signals with respect to the lag in transmitted angles. When it comes to an aberrated image, speckle is highly decorrelated and the angular coherence of backscattered signals sinks very quickly from an angle to the next one. After SVD filtering of the image, this effect is totally recovered, and even further since the angular coherence of each block is constant equal to 1. Even if this result seems certain mathematically, it illustrates that the SVD provides an image, for which all pixels are being seen the same way by all transmit angles.

Compared to the raw image, the numerically aberrated image showed a strong degradation (Fig. 6 (a) and (b)), that is fully recovered after SVD-beamforming correction (Fig. 6 (c)). The lateral resolution, evaluated on reflecting pins, is effectively improved from 1.02 mm to 0.88 mm. Also,

the contrast on the anechoic cyst in speckle is enhanced up to 11.7 dB, and reaches the contrast of the non-aberrated image. When the simulated law is directly defined in the plane wave space, the SVD-beamformer result is shown to be very consistent with the introduced phase change (Fig.6 (d), $r^2 = 99\%$). When the simulated aberration law is defined in the canonical space, we used synthetic aperture acquisitions to reconstruct the realistic aberration. Then, we built the ultrafast compound matrix and extracted the phase of the first angular singular vector. This gave us an angular aberration law, which was projected in the element space to be compared with the true numerical aberration (Fig. 6 (e)). Both laws are in very good agreement with a coefficient of determination $r^2 = 98\%$. This validates the ability of our method, on simulated examples, to retrieve realistic aberrations initially defined either in canonical or in plane wave basis.

Even if the numerical aberration is not fully distributed in the medium but rather a phase screen, we did perform the SVD-beamforming on different geometrical patches. We selected in the images different patches containing only speckle (no reflectors nor anechoic areas). Fig. 6 (d) and (e) show that the phase laws extracted from this patch-SVD (corresponding to V_1^*) are consistent with the expected numerical aberrations. This demonstrates that the efficiency of

TABLE I

RESUME OF THE RESULTS OF SVD BEAMFORMER ON IN VITRO ABERRATED PHANTOM, WITH 50 ABERRATING PHASE SCREENS TESTED. SPECKLE BRIGHTNESS ABERRATION CORRECTION WAS ALSO IMPLEMENTED TO COMPARE THE CORRECTION EFFECTS

	SVD Beamformer	Speckle Brightness
Mean aberration law correlation (r²)	**0.9935**	**0.6727**
Contrast on initial image	-28.2 dB	
Mean contrast after aberration ± std	-18.7 ± 4.1 dB	
Mean contrast after correction ± std	-28.2 ± 0.3dB	-21.1 ± 0.9dB
Mean contrast improvement	**9.5 dB**	**2.4 dB**
Target width on initial image	0.54 mm	
Target width on aberrated image	0.70 ± 0.14 mm	
Target width after correction ± std	0.57 ± 0.005 mm	0.64 ± 0.08 mm
Mean resolution improvement	**22.8 %**	**9.4 %**

the aberration law extraction does not rely on the presence of coherent targets within the patch and only requires speckle.

We further tested 50 different numerical aberrators to assess the ability of SVD beamforming to correct strong and highly variable dephasing screens. We used, as numerical aberration laws, some randomized linear combinations of linear, parabolic and sinusoidal phase laws. The order of magnitude was chosen to be consistent with typical *in vivo* aberrating layers, up to few tens of microseconds. The correlation length of the tested phase laws varied randomly from 5 to 20 angles.

We added to the results a comparison with another existing aberration correction: we indeed implemented Speckle Brightness approach as described in [19]. A first speckle brightness value was calculated on the aberrated image. For a given array element, the RF signal was delayed of 0.2λ at emission and reception in beamforming. Speckle brightness was then recalculated on the obtained image. If the speckle brightness increased, the RF delay was incremented of $+0.2\lambda$ (-0.2λ if it decreased). The process was iterated until a maximal value of speckle brightness was reached. This was repeated for each element of the transducer. Finally, beamforming with optimal delays gave the corrected image. We performed both methods on the exact same set of aberrated data and retrieved the results in Table I. First we observe, with the r^2 value, that the SVD beamformer is very efficient to recall the aberration law. Also, both contrast (-9.5 dB) and resolution (-22.8%) improve significantly with SVD beamforming. These improvements clearly outperform speckle brightness method. The low standard deviations demonstrate that the SVD beamforming approach gives confident results regardless the numerical aberration.

B. SVD Beamforming in Speckle Noise With Physical Aberrators

These improvements of the SVD beamformer are visible as well on physically aberrated data (Fig. 7). As the non-negligible thickness of the aberrator tends to decrease the isoplanatic angle, the SVD processing is now performed on many different isoplanatic patches. After SVD beamforming, reflecting pins resolution improved from 2.1mm to 1.3mm, and contrast increased by 8.5 dB+/− 1.9 dB.

We were also able to compare the aberration law extracted from the SVD patch correction and its true estimation - obtained by using the backscattered wavefront coming from the closest pin. We found again a very good agreement ($r^2 = 95\%$) between those two angular aberration laws. In the case of a thick aberrating lens, smaller isoplanatic patches were used to perform the correction, in order to keep the aberration correction as optimal as possible on the patch spatial extension. An interesting issue remains in the optimization of this patch size in order to perform the most efficient possible correction. In order to investigate this point, we designed patches around a central point of five different sizes, and performed correction on each of them with SVD beamforming (Fig. 7).

C. Influence of the Patch Size on Aberration Correction

In order to validate our method, and identify the patch sizes providing a realistic result, we considered a speckle phantom image containing a single reflecting pin at its center (Fig. 8. (a)).

First, we used the backscattered signal coming from the reflecting pin at the center of our image. From these RF data, we extracted the aberration delay law in the element space. We used the matrix P defined in part II.C. to project the canonical law into the plane wave basis. This gave us an estimation of the physical aberration encountered in the region surrounding the reflector, and is displayed on Fig. 8.(f).

Then, we defined a small patch ($25\lambda \times 30\lambda$, Fig. 8 (b)), a median patch ($35\lambda \times 45\lambda$, Fig. 8 (c)), and a large patch ($50\lambda \times 100\lambda$, Fig. 8 (d)) surrounding the reflector. For the SVD-beamforming operation, we excluded the reflecting pin area at the center of the patch in order to rely only on speckle noise. For the small, and median patches, the phase of the first angular singular vector retrieves the same result in terms of aberration and image correction. That means that for these patch sizes, the patch is seeing the same aberrator and the SVD-beamformer provides an optimal correction and estimation of the aberration. When increasing the patch size, we observe a change in the phase. The spatial extent becomes then too large to ensure a correct solution for the SVD beamformer. Indeed, the aberration can no longer be considered similar for all pixels of the patch, and it is logical that the SVD performance degrades. In the opposite case, for a too small patch, the number of pixels would not be sufficient for the SVD to extract the correct aberration law. One can see that for the smaller patch sizes, the physical aberration
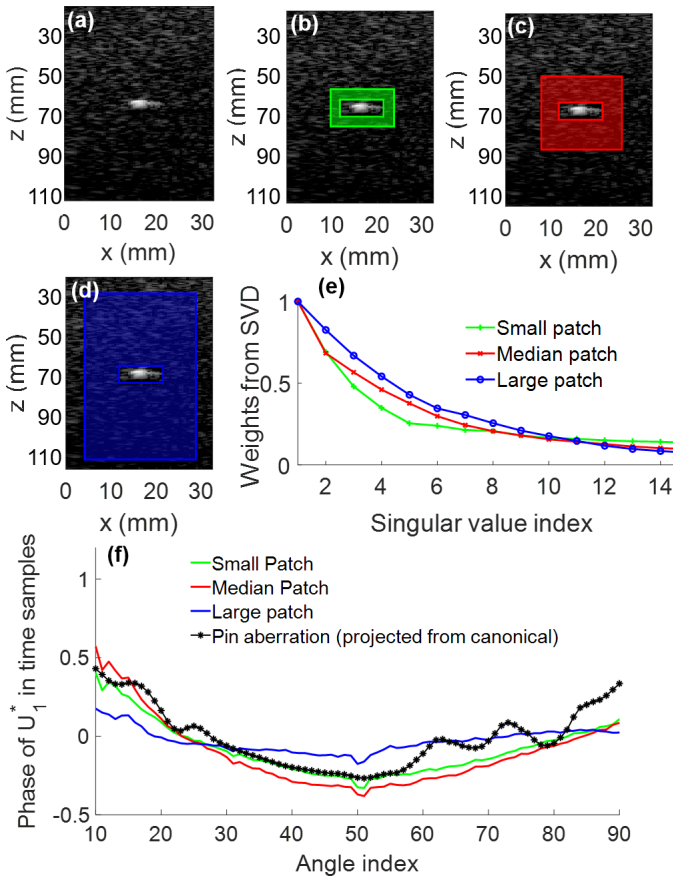
Fig. 8. (a) B-mode image of a phantom containing speckle and one reflecting pin. (b) Small patch definition: $[25\lambda \times 30\lambda]$ region excluding the central reflecting pin (c) Median patch definition: $[35\lambda \times 45\lambda]$ region excluding the central reflecting pin (d) Large patch definition: $[50\lambda \times 100\lambda]$ region excluding the central reflecting pin (e) Normalized eigenvalues distribution for each patch size (zoomed for low eigen indices). (f) Angular aberration laws extracted from SVD beamformer for a small patch compared to the experimental canonical aberration obtained from the central pin and then projected in plane wave space.
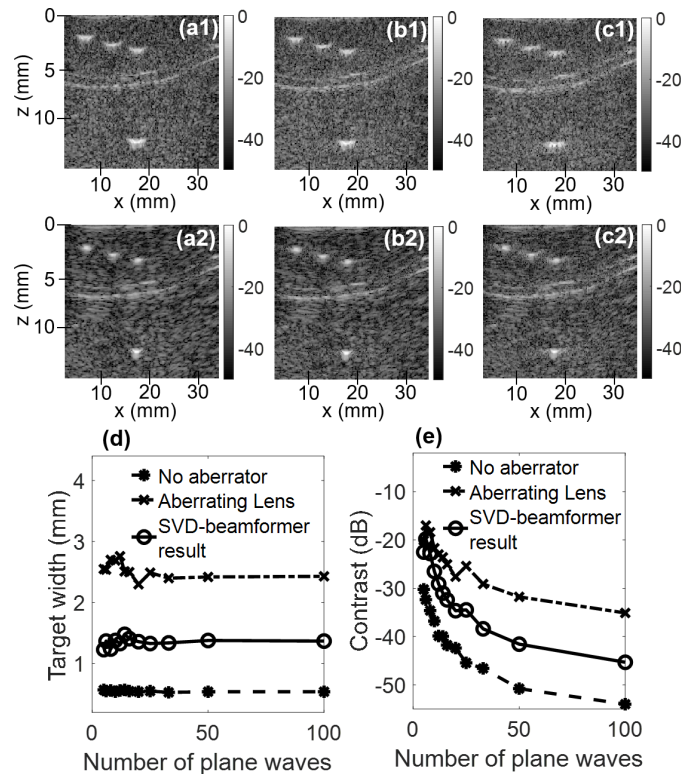

Fig. 9. Impact of lowering the amount of plane wave transmits on SVD beamforming for an aberrated pin phantom (1 = result of the compound, 2 = result of SVD beamformer). (a) 100 plane wave images, (b) 10 plane waves images, (c) 5 plane wave images, (d) Evolution of the resolution and contrast after correction with SVD beamforming on different amount of plane waves. Contrast was estimated on an anechoic inclusion acquired with the same aberrator.

estimation is in good agreement with the SVD-Beamformer results.

For this case, we are thus able to identify a typical patch size for aberration correction. It is actually the highest size for which the phase laws remain consistent. This optimization of the patch size can be done by looking at the singular value distribution of the SVD for different sizes. Fig. 8 (e) shows that the singular value distribution drops rapidly to zero for a correct patch size, whereas in the case of too large patches, the slope at the origin is less steep. The ratio between the first and second singular value of the Ultrafast Compound Matrix can be considered as an interesting parameter to choose the size of isoplanatic patch. In the case of the time reversal operation H^tH^*, such ratio was shown of particular importance as it affects the convergence of iterative time reversal processing [26], [33].

D. Influence of the Number of Plane Wave Transmissions

The previous results showed that, for an appropriate patch size, the SVD beamformer allows us to retrieve both the aberration law and the image correction. Though, this last effect should decrease when less plane waves are transmitted. The SVD operation is indeed more efficient when the decomposition basis is larger. Therefore, we tested different acquisitions with various amount of plane wave transmits on aberrated phantoms. Fewer angles gives less angular frequency components to describe the phase law, but we still see an improvement in the first singular vector image. Fig. 9 shows in (a), (b), (c) the comparison of the aberrated image, and the SVD-beamformed image for different amount of plane wave transmits. We estimated, with the same aberrator in both cases, the lateral resolution on the pin phantom, and the contrast on an anechoic inclusion.

We compared, on the graph (d) of Fig. 9, the correction efficiency as a function of transmitted plane waves. For all configurations with different number of plane wave transmissions, the SVD beamformer improves the image quality both for contrast and resolution. Contrast improvement decreases progressively, whereas there is a clear drop of resolution improvement around 6 transmits. Still, one can note that even for as low as 5 plane waves, the resolution keeps getting better with the SVD correction even if it is less remarkable on contrast. It is therefore a matter of trade-off between the frame rate expected (amount of transmitted plane waves) and the efficiency of the correction. The chosen configuration will essentially depend on the clinical application.
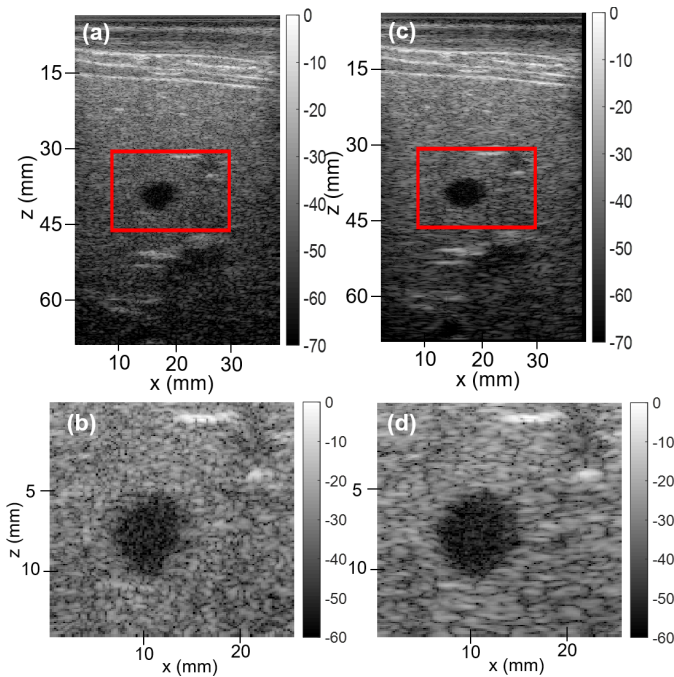
Fig. 10. In vivo B-mode results on liver. Acquisitions of 41 transmitted plane waves: (a) Classical compound beamforming showing red-squared region. (b) Renormalized Bmode of the anechoic vessel area. (c) Result of SVD-beamforming on the whole image. (d) Result of SVD-beamforming in the region of interest.

TABLE II

CALCULATION TIMES FOR AN IMAGE - BEAMFORMED AT $\lambda/2$ - ACQUIRED AT A CENTRAL FREQUENCY OF 6.25 MHz AND A SAMPLING FREQUENCY OF 25 MHz, AT 5cm DEPTH WITH A 192-ELEMENT PROBE. CALCULATIONS WERE COMPUTED ON A PC WITH AN INTELCOREI7-5820K CPU (3.30GHz), 32 GO RAM, ON A GRAPHICS PROCESSING UNIT: GEFORCE GTX 1080 TI

Processing	Time for processing (s)			
Number of patch(es)	1	9	25	100
Size of patch (pixels)	592*192	196*63	117*37	58*18
Beamforming 100 angles	0.000036			
SVD-correction 100 angles	0.50	0.41	0.34	0.50
SVD-correction 10 angles	0.025	0.018	0.023	0.045
SVD-correction 5 angles	0.012	0.010	0.014	0.029

E. In Vivo SVD Beamforming in the Human Liver

Finally, we tested our SVD beamforming on in vivo data. The ultrasound emission sequences were calibrated with the acoustic measurement system from Acertara Acoustic Laboratories. Both the spatial peak time-average (ISPTA) and the Mechanical Index (MI) were shown to be, in all considered cases, below FDA Track 3 Recommendations (ISPTA = 720mW/cm^2 and MI = 1.9). Indeed, maximum values obtained with our sequences were respectively ISPTA = 254.2 mW/cm^2, and MI = 0.819.

This allowed us to perform our acquisitions on liver of a healthy volunteer. Fig. 10 shows Bmode comparison of classical compounded image, and SVD-beamformed image. The overall quality of the image improves with a contrast enhancement of 4.78 dB. Interestingly, some structures that were difficult to image in classical compound, tend to be more visible in the corrected image. These preliminary in vivo results show the reliability of the proposed method to correct more spatially distributed aberrators. This is therefore a promising first step towards clinical use of SVD-beamformer for adaptive imaging of patients.

V. DISCUSSION

The results presented above demonstrate that the SVD beamformer is a reliable and efficient technique to correct images and retrieve simultaneously the phase aberration law from ultrafast data acquired using plane wave compounding. In vitro experiments in tissue mimicking phantoms have shown both a 9.5 dB+/− 0.9 dB rise in contrast for simulated aberrations and a 8.5 dB+/− 1.9 dB contrast rise for physical aberrations. The lateral resolution was also improved in both cases respectively from 0.7mm to 0.57mm in the simulated aberrations case, and from 2.1mm to 1.3mm with the physical aberration. Another simple way to assess the accuracy of our method in retrieving the aberration pattern was to beamform raw data while correcting the phase and amplitude aberrations determined by SVD, and to re-perform the SVD beamforming process on this new set of corrected data. As expected, this resulted in a flatten phase distribution, as if no aberration had distorted the corrected backscattered signals. This showed also that a single round of correction was required whereas existing methods often imply iterative processes. Of particular interest is the simplicity and straightforward implementation of this SVD beamforming. Using parallel computation devices, and high-end processors, the implementation time of our method is significantly low enough to perform real-time aberration correction. It depends on the number of transmit angles in the data, but also on the size of the isoplanatic patches for Singular Value Decomposition. We showed in Fig. 9, that for a reasonable amount of plane waves, and for a patch size of tens of λ in axial and lateral directions, the computation speed is yet high enough to correct in real-time the beamformed data which is a major advantage of this SVD beamformer.

We believe that the computation time could be even further reduced by optimizing the parallelization of the algorithms. This allows us, already, to consider novel applications such as real-time adaptive functional imaging, motion-correction on cardiac imaging, or transcranial Doppler imaging of the brain.

Also, we present here computation times for small number of angles. Though, too few transmit angles will inexorably lead to a weaker performance of Singular Value Decomposition, Fig. 9 shows the performance of the correction depending on the number of transmitted plane waves. Interestingly, the SVD beamformer improves the image quality – both in terms of resolution and contrast - up to a quite small number

of angles (typically 10 to 20 angles). Even in the extreme case of N=5 plane waves, the SVD beamformer leads to an improvement of resolution nevertheless without any contrast gain anymore. In this case, it is due to the lower number of available orthonormal basis vectors insufficient to fully describe the aberrator.

For transcranial imaging, it could seem limitative that our method only corrects in emission. Though, due to time-reversal symmetry of the wave equation, the aberration is also symmetric. It is therefore possible to correct in emission, as well as in reception by re-beamforming the data while taking the aberration delay into account in both propagation ways. To consider the aberration phase in reception, the delay law would need to be expressed in the canonical basis. This can be obtained by a change-of-basis thanks to the matrix P introduced in II-C. We performed tests on simulated delay laws, and observed that the law remains highly consistent down to a dozen transmit angles. For lower number of angles, the projection of the estimated angular aberration in the canonical basis fails to reach the true aberration. This is a limitation, for now, to the ultrafast character of the adaptive beamforming when both transmit and receive correction are desired.

Another limitation of our technique relies on the assumption of near field phase screen aberrator. Despite longstanding research in the field of aberration corrections, this assumption has been shown insufficient to correct phase aberration in a way that is significant meaningful for diagnostic image quality *in vivo*. The use of a near screen phase screen layer fails to model spatially distributed aberrations which is the vast majority of cases in biomedical applications. Nevertheless, in the case of reasonable medium heterogeneities such as soft tissues, the description of a complex distributed aberrator as a large set of phase screen aberrators corresponding to spatially distributed isoplanatic patches permits to model aberrations more complex than a near-field aberrator. The optimization of the number of isoplanatic patches and their overlapping for the final image reconstruction was not discussed in the manuscript but it is also an interesting problem with room of further improvements. The size of the isoplanatic region depends on geometric parameters (such as depth, aperture) and aberration characteristics (such as correlation length). Indeed, the more distributed the aberrator is, the smaller the isoplanatism angle is and consequently the smaller the isoplanatic patch should be. For smaller isoplanatic patches, the standard deviation in the aberration estimation increases as less pixels are available to stabilize the SVD processing. Though, we observed on Fig. 8 that there is a trade-off to find between the stability of the angular aberration correction and the size of the patch chosen for SVD to perform an efficient correction. To date, we decided to choose a typical $20\lambda \times 40\lambda$ patch size for the SVD beamforming of data with our silicone aberrating lens and its geometry. For the *in vivo* liver experiment, we chose a $10\lambda \times 70\lambda$ patch size. The determination of the ideal patch size highly depends on experimental conditions and could be refined in further works. A 50% overlapping between patches was chosen and the final image was reconstructed by choosing for each pixel the mean value of the same pixel in the several overlapping patches.
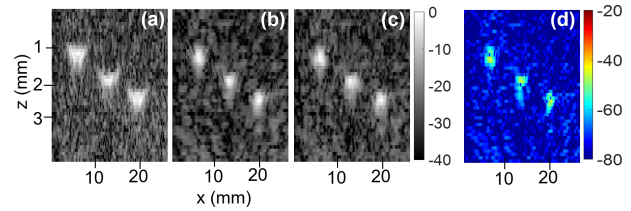

Fig. 11. (a) Raw aberrated image of reflecting pins in speckle. (b) Corrected image after SVD-beamforming. (c) Image only rephased with the aberration extracted from SVD-beamforming (no filtering). (d) Difference between images (b) and (c), normalized by image (c) intensity.

This enables to avoid spatial discontinuities at the frontier between patches. Other weighting methods before summation over the different patches could be studied in further works in order to optimize the computation time.

Since it is the common configuration in clinical ultrasound applications, we used in this work a λ-pitch linear array. However, it has been shown that using $\lambda/2$-pitch probes can decrease the number of required emissions in plane wave imaging, and improve the image quality by reducing grating lobes in the near-field of the ultrasonic probe [34]. As it would also reduce the field of view for a similar number of elements, the probe choice depends mostly on the clinical application. Further work will thus be needed to fully investigate the capability of the SVD-beamformer for different probe geometries such as curved or phased arrays.

One important point to notice is that the SVD beamformer also goes beyond a phase and amplitude aberration correction. Indeed, for each patch, the final SVD image corresponding to the first singular vector U_1 does not correspond to the simple phase delaying and summation of the initial data. In other words, the SVD processing performs a more complex aberration correction than just a phase screen aberrator correction. Fig. 11 illustrates this important point. It compares the corrected image provided by SVD with the corrected image provided when applying only a phase correction delay during the conventional coherent compounding process. The difference between both corrected images in terms of normalized amplitude (Fig. 11 (c)) is non negligible. It shows that SVD beamforming improves also the speckle grain. There is therefore a filtering effect of the SVD beamformer that retrieves only the most coherent data from different plane wave transmits.

In our study, we considered a simple scattering regime for the backscattered signals. This hypothesis is sufficient in most configurations of biomedical ultrasound. Nevertheless, the discrimination between signals resulting from simple and multiple scattering could be performed at a non-negligible supplemental computational cost before our SVD beamforming method by studying the propagation matrix singular vectors [35].

In the case of a non-aberrated medium, for a correct image, the first angular eigen vector out of SVD exhibit obviously a constant phase at 0. Though, if there is a mismatch between the beamforming sound speed and the medium sound speed, the phase immediately shows a hyperbolic trend – either

convex or concave depending on the sign of the error. So, the phase of the eigen value straightforwardly informs on the sound speed accuracy in the patch of interest. The framework of this SVD beamformer processing is thus particularly adapted for quantitative imaging, and particularly acoustic sound speed mapping.

VI. Conclusion

The SVD Beamformer provides a fast and adaptive method for beamforming whilst correcting phase and amplitude aberrations. On a theoretical point of view, applying the SVD on a particularly suited ultrafast compound Matrix R gives a straightforward solution to the aberration correction problem. This technique for adaptive ultrasound imaging reunites Phase Aberration Correction and Coherence-based imaging in a single correction operation. Selecting the first image singular vector is sufficient to maximize the angular coherence between transmitted insonifications and enhances the image quality, without compromising very high frame rate imaging. We propose for the first time a physical meaning to the mathematical SVD operation in the context of ultrasound image formation. Future work will focus on the application of this technique for quantitative ultrasound imaging.

References

[1] C. Bruneel, R. Torguet, K. M. Rouvaen, E. Bridoux, and B. Nongaillard, "Ultrafast echotomographic system using optical processing of ultrasonic signals," *Appl. Phys. Lett.*, vol. 30, no. 8, pp. 371–373, 1977.

[2] S. W. Smith, H. G. Pavy, and O. T. von Ramm, "High-speed ultrasound volumetric imaging system. I. Transducer design and beam steering," *IEEE Trans. Ultrason., Ferroelectr., Freq. Control*, vol. 38, no. 2, pp. 100–108, Mar. 1991.

[3] J.-Y. Lu, "2D and 3D high frame rate imaging with limited diffraction beams," *IEEE Trans. Ultrason., Ferroelectr., Freq. Control*, vol. 44, no. 4, pp. 839–856, Jul. 1997.

[4] J.-Y. Lu, "Experimental study of high frame rate imaging with limited diffraction beams," *IEEE Trans. Ultrason., Ferroelectr., Freq. Control*, vol. 45, no. 1, pp. 84–97, Jan. 1998.

[5] M. Tanter, J. Bercoff, L. Sandrin, and M. Fink, "Ultrafast compound imaging for 2-D motion vector estimation: Application to transient elastography," *IEEE Trans. Ultrason., Ferroelectr., Freq. Control*, vol. 49, no. 10, pp. 1363–1374, Oct. 2002.

[6] S. I. Nikolov and J. A. Jensen, "*In-vivo* synthetic aperture flow imaging in medical ultrasound," *IEEE Trans. Ultrason., Ferroelectr., Freq. Control*, vol. 50, no. 7, pp. 848–856, Jul. 2003.

[7] G. Montaldo, M. Tanter, J. Bercoff, N. Benech, and M. Fink, "Coherent plane-wave compounding for very high frame rate ultrasonography and transient elastography," *IEEE Trans. Ultrason., Ferroelectr., Freq. Control*, vol. 56, no. 3, pp. 489–506, Mar. 2009.

[8] M. Tanter and M. Fink, "Ultrafast imaging in biomedical ultrasound," *IEEE Trans. Ultrason., Ferroelectr., Freq. Control*, vol. 61, no. 1, pp. 102–119, Jan. 2014.

[9] G. E. Trahey and S. W. Smith, "Properties of acoustical speckle in the presence of phase aberration part I: First order statistics," *Ultrason. Imag.*, vol. 10, no. 1, pp. 12–28, Jan. 1988.

[10] M. Jaeger, E. Robinson, H. G. Akarçay, and M. Frenz, "Full correction for spatially distributed speed-of-sound in echo ultrasound based on measuring aberration delays via transmit beam steering," *Phys. Med. Biol.*, vol. 60, no. 11, pp. 4497–4515, Jun. 2015.

[11] M. Jaeger, G. Held, S. Peeters, S. Preisser, M. Grünig, and M. Frenz, "Computed ultrasound tomography in echo mode for imaging speed of sound using pulse-echo sonography: Proof of principle," *Ultrasound Med. Biol.*, vol. 41, no. 1, pp. 235–250, Jan. 2015.

[12] M. O'Donnell and S. W. Flax, "Phase-aberration correction using signals from point reflectors and diffuse scatterers: Measurements," *IEEE Trans. Ultrason., Ferroelectr., Freq. Control*, vol. UFFC-35, no. 6, pp. 768–774, Nov. 1988.

[13] G. Montaldo, M. Tanter, and M. Fink, "Time reversal of speckle noise," *Phys. Rev. Lett.*, vol. 106, no. 5, pp. 1–4, Feb. 2011.

[14] B.-F. Osmanski, G. Montaldo, M. Tanter, and M. Fink, "Aberration correction by time reversal of moving speckle noise," *IEEE Trans. Ultrason., Ferroelectr., Freq. Control*, vol. 59, no. 7, pp. 1575–1583, Jul. 2012.

[15] N. Q. Nguyen and R. W. Prager, "A spatial coherence approach to minimum variance beamforming for plane-wave compounding," *IEEE Trans. Ultrason., Ferroelectr., Freq. Control*, vol. 65, no. 4, pp. 522–534, Apr. 2018.

[16] R. Mallart and M. Fink, "The van Cittert–Zernike theorem in pulse echo measurements," *J. Acoust. Soc. Amer.*, vol. 90, no. 5, pp. 2718–2727, Nov. 1991.

[17] M. A. Lediju, G. E. Trahey, B. C. Byram, and J. J. Dahl, "Short-lag spatial coherence of backscattered echoes: Imaging characteristics," *IEEE Trans. Ultrason., Ferroelectr., Freq. Control*, vol. 58, no. 7, pp. 1377–1388, Jul. 2011.

[18] J. Dahl, "Coherence beamforming and its applications to the difficult-to-image patient," in *Proc. IEEE Int. Ultrason. Symp. (IUS)*, Sep. 2017, pp. 1–7.

[19] L. Nock, G. E. Trahey, and S. W. Smith, "Phase aberration correction in medical ultrasound using speckle brightness as a quality factor," *J. Acoust. Soc. Amer.*, vol. 85, no. 5, pp. 1819–1833, May 1989.

[20] Y. L. Li and J. J. Dahl, "Coherent flow power Doppler (CFPD): Flow detection using spatial coherence beamforming," *IEEE Trans. Ultrason., Ferroelectr., Freq. Control*, vol. 62, no. 6, pp. 1022–1035, Jun. 2015.

[21] M. Imbault *et al.*, "Robust sound speed estimation for ultrasound-based hepatic steatosis assessment," *Phys. Med. Biol.*, vol. 62, no. 9, pp. 3582–3598, May 2017.

[22] A. Aubry and A. Derode, "Detection and imaging in a random medium: A matrix method to overcome multiple scattering and aberration," *J. Appl. Phys.*, vol. 106, no. 4, Aug. 2009, Art. no. 044903.

[23] Y. L. Li and J. J. Dahl, "Angular coherence in ultrasound imaging: Theory and applications," *J. Acoust. Soc. Amer.*, vol. 141, no. 3, pp. 1582–1594, Mar. 2017.

[24] F. Vignon, J. S. Shin, S.-W. Huang, and J.-L. Robert, "Adaptive ultrasound clutter rejection through spatial eigenvector filtering," in *Proc. IEEE Int. Ultrason. Symp. (IUS)*, no. 1, Sep. 2017, pp. 31–34.

[25] J.-L. Robert and M. Fink, "Green's function estimation in speckle using the decomposition of the time reversal operator: Application to aberration correction in medical imaging," *J. Acoust. Soc. Amer.*, vol. 123, no. 2, pp. 866–877, Feb. 2008.

[26] C. Prada and M. Fink, "Eigenmodes of the time reversal operator: A solution to selective focusing in multiple-target media," *Wave Motion*, vol. 20, no. 2, pp. 151–163, Sep. 1994.

[27] G. Montaldo, M. Tanter, and M. Fink, "Real time inverse filter focusing by iterative time reversal," *J. Acoust. Soc. Amer.*, vol. 112, no. 5, p. 2446, Nov. 2002.

[28] M. Tanter, J.-L. Thomas, and M. Fink, "Focusing and steering through absorbing and aberrating layers: Application to ultrasonic propagation through the skull," *J. Acoust. Soc. Amer.*, vol. 103, no. 5, pp. 2403–2410, May 1998.

[29] M. Tanter, J.-L. Thomas, and M. Fink, "Time reversal and the inverse filter," *J. Acoust. Soc. Amer.*, vol. 108, no. 1, pp. 223–234, Jul. 2000.

[30] M. Tanter, J.-F. Aubry, J. Gerber, J.-L. Thomas, and M. Fink, "Optimal focusing by spatio-temporal inverse filter. I. basic principles," *J. Acoust. Soc. Amer.*, vol. 110, no. 1, pp. 37–47, Jul. 2001.

[31] J.-F. Aubry, M. Tanter, J. Gerber, J.-L. Thomas, and M. Fink, "Optimal focusing by spatio-temporal inverse filter. II. Experiments. Application to focusing through absorbing and reverberating media," *J. Acoust. Soc. Amer.*, vol. 110, no. 1, pp. 48–58, Jul. 2001.

[32] F. Chassat, "Theoretical evaluation of the isoplanatic patch of an adaptive optics system working through the atmospheric turbulence," *J. Opt.*, vol. 20, no. 1, pp. 13–23, Jan. 1989.

[33] C. Prada, J. Thomas, and M. Fink, "The iterative time reversal process: Analysis of the convergence," *J. Acoust. Soc. Amer.*, vol. 97, no. 1, pp. 62–71, Jan. 1995.

[34] J. Jensen, M. B. Stuart, and J. A. Jensen, "Optimized plane wave imaging for fast and high-quality ultrasound imaging," *IEEE Trans. Ultrason., Ferroelectr., Freq. Control*, vol. 63, no. 11, pp. 1922–1934, Nov. 2016.

[35] A. Aubry and A. Derode, "Singular value distribution of the propagation matrix in random scattering media," *Waves Random Complex Media*, vol. 20, no. 3, pp. 333–363, Aug. 2010.